Effective Low Magnetic Field $J_c(B)$ Scaling of ITER Nb_3Sn Strands by Magnetization and Critical Current Measurements

Jianfeng Huang, Yury Ilyin, Denis Bessette, Chao Zhou, Ruben Lubkemann, Cris Vermeer, W. A. J. Wessel, and Arend Nijhuis

***Abstract*—For the International Thermonuclear Experimental Reactor magnets, a significant fraction of the Nb_3Sn conductors will be operating at a low field ($B < 4$ T), such as the outer turns of the central solenoid modules and toroidal field winding packs, while so far, the $I_c(B,T,\varepsilon)$ parameterization has been derived from measurements carried out at higher fields ($B \geq 7$ T). It may not be accurate enough to adopt this parameterization for the extrapolation of the conductors' operating performance in terms of critical current (I_c) and current sharing (T_{cs}). The critical current characteristic can be effectively extended to the lower field region by means of a relation between the magnetization and critical current. The parameterization of the derived critical current scaling law $J_c(B)$ is processed for the field range of the magnetization measurement ($0 < B \leq 9$ T) and the critical current measurements ($7 \leq B < 12$ T) in order to cover the full range up to 12 T.**

***Index Terms*—Nb_3Sn, critical current, hysteresis loss, International Thermonuclear Experimental Reactor (ITER), magnetization, parametrization.**

I. Introduction

THE magnet system of the International Thermonuclear Experimental Reactor (ITER) consists of 18 toroidal field (TF) coils, 6 central solenoid (CS) modules, 6 poloidal field (PF) coils, and 18 correction coils (CCs) of which the PF and CC coils are wound with NbTi superconducting strands and the TF and CS coils are wound with Nb_3Sn strands [1], [2]. For the ITER Nb_3Sn strands, 6 ITER partners [so-called Domestic Agencies (DAs)] are in charge of the procurement, and 11 companies have carried out the specific manufacturing tasks under the supervision of the ITER Organization and DA's, 8 for the TF coils and 3 for the CS coils. Furthermore, two types of producing processes are accepted for the ITER Nb_3Sn strands—the bronze route (BR) and internal-tin (IT) processes. Four TF and two CS strands are made by the BR process, and the rest are made by the IT process [3].

The specification of both the TF and CS Nb_3Sn strands is shown in Table I. During the operation of the ITER machine, a significant fraction of the Nb_3Sn conductors will be operating at a low field ($B < 4$ T), such as the outer turns of the CS modules and TF winding packs, while so far the $I_c(B, T, \varepsilon)$ parameterization has been derived from measurements carried out at a higher field ($B \geq 7$ T) [4]. This parameterization has been adopted to assess the operating performance of the conductors in terms of critical current (I_c) and current-sharing temperature (T_{cs}). It may not be accurate enough to use the existing $I_c(B, T, \varepsilon)$ parameterization for extrapolation to the lower field region for analysis purposes, in particular, for a proper evaluation of the hysteresis losses of the Nb_3Sn coils during the plasma operating scenario. A similar characterization work has been carried out previously by CERN concerning five Nb_3Sn strands and here a comparable approach is followed [5].

In total, one CS and six TF type of ITER Nb_3Sn strands have been tested at the University of Twente, of which three are BR and four are IT processed. They are manufactured by seven companies, and named TFBR01, TFBR02, TFIT01, TFIT02, TFIT03, TFIT04, and CSBR01, respectively. In this article, the measurement and analysis of the hysteresis loss and the critical current are described.

II. Experimental Setup and Sample Preparation

The aim is to extend the critical current $J_c(B)$ law at the whole magnetic field region from 0 to 12 T. Therefore, besides the critical current derived from transport current measurements at fields $7 \leq B \leq 12$ T, magnetization measurements are performed with a vibrating sample magnetometer (VSM), at the field region $0 < B \leq 9$ T; thus, there is an overlapping field from 7 to 9 T. The Nb_3Sn is a brittle A15 material formed during a heat treatment reaction; thus, the winding of the strands should be done prior to the Nb–Sn reaction. For the bronze routed strands,

Manuscript received 5 September 2021; revised 30 January 2022, 2 May 2022, and 22 June 2022; accepted 6 July 2022. Date of publication 14 July 2022; date of current version 9 August 2022. This work was supported by ITER IO, Cadarache, France, within the framework of the ITER service contract: Test and Analysis of ITER Coil Joints, under Grant ITER/CT/13/4300000762. This article was recommended by Associate Editor C. Luongo. *(Corresponding author: Jianfeng Huang.)*

Jianfeng Huang, Ruben Lubkemann, Cris Vermeer, W. A. J. Wessel, and Arend Nijhuis are with the Faculty of Science and Technology, University of Twente, 7522 NB Enschede, The Netherlands (e-mail: j.huang-2@utwente.nl; ruben@foundationsuperact.org; c.h.vermeer@foundationsuperact.org; w.a.j.wessel@utwente.nl; a.nijhuis@utwente.nl).

Yury Ilyin and Denis Bessette are with ITER Organization, 13115 St. Paul-lez-Durance, France (e-mail: yury.ilin@iter.org; denis.bessette@iter.org).

Chao Zhou was with the Faculty of Science and Technology, University of Twente, 7522 NB Enschede, The Netherlands. He is now with the Institute of Plasma Physics, Chinese Academy of Sciences, Hefei 23000, China (e-mail: c.zhou@utwente.nl).

Color versions of one or more figures in this article are available at https://doi.org/10.1109/TASC.2022.3190921.

Digital Object Identifier 10.1109/TASC.2022.3190921

TABLE I
TF AND CS Nb_3Sn STRAND SPECIFICATION AND ACTUAL ACHIEVED VALUES [6]–[8]

	TF		CS
	Bronze routed	Internal tin	Bronze routed
Outer diameter	0.82 mm ± 5 µm	0.82 mm ± 5 µm	0.83 mm ± 5 µm
Strand twist pitch	15 ± 2 mm	15 ± 2 mm	15 ± 2 mm
Hard Cr-coating	2 + 0/− 1 µm	2 + 0/− 1 µm	2 + 0/− 1 µm
I_c at 12 T, 4.2 K	190–255 A	240–315 A	>260 A
Hysteresis loss on a ±3 T field cycle (4.2 K)	40–500 kJ/m^3	180–600 kJ/m^3	≤500 kJ/m^3
n-value at 12 T, 4.2K	>20	>20	>20
Residual resistivity ratio	>100	>100	>100
Cu:nonCu	1.0 ± 0.1	1.0 ± 0.1	1.0 ± 0.1

TABLE II
HEAT TREATMENT SCHEDULE OF THE STRAND SAMPLES

Sample	Heat treatment cycle	RRR
TFBR01	595 °C (160 h) – 620 °C (320 h)	117
TFBR02	570 °C (250 h) – 650 °C (100 h)	150-170
CSBR01		146
TFIT01	210 °C (50 h) – 340 °C (25 h) – 450 °C (25 h) – 575 °C (100 h)– 650 °C (100 h)	158
TFIT02		170
TFIT03	210 °C (50 h) – 340 °C (25 h) – 450 °C (25 h) – 575 °C (100 h)– 650 °C (120 h)	138
TFIT04	210 °C (50 h) – 340 °C (25 h) – 450 °C (25 h) – 575 °C (100 h)– 650 °C (200 h)	>150

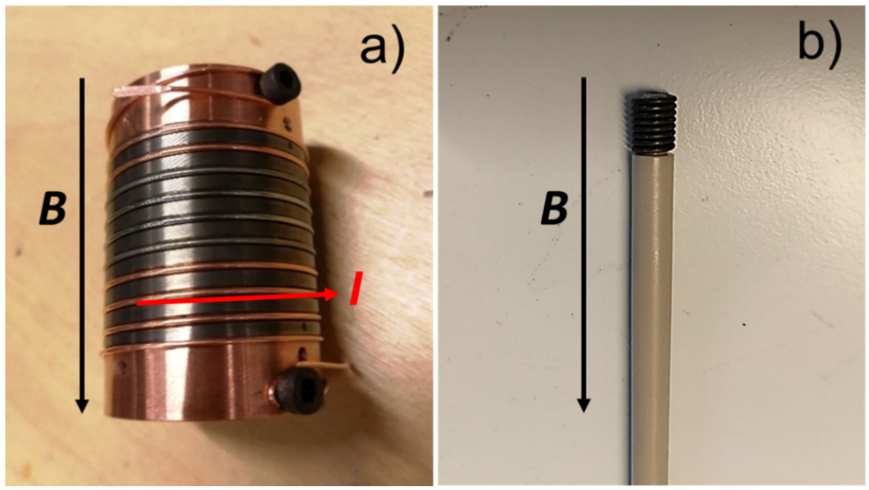

Fig. 1. Photographs of (a) ITER-type VAMAS sample for heat treatment and critical current measurement and (b) minicoil sample assembled on the probe for the VSM measurement after heat treatment.

the Nb_3Sn layers are typically formed around each original Nb filament embedded in the bronze matrix. The IT processed strands consist of three main composites: Cu, Sn, and Nb. During the heat treatment, the Cu and Sn elements are first converted into high-Sn bronze phases at temperatures up to about 500 °C, and then react with the Nb filaments after the temperature is heated up to 600–700 °C [9]. The specific heat treatment schedules for the seven samples are shown in Table II.

For the transport critical current measurement, the strand is wound on a standard ITER-type VAMAS barrel [10], which is a molybdenum sulfide coated and preoxidized Ti6Al4V cylinder with a spiral groove and two copper end caps. The coefficient of thermal expansion of Ti6Al4V matches closely that of Nb_3Sn. The outer cylinder diameter is 32 mm and the height is 28.6 mm [11], as shown in Fig. 1(a). After the heat treatment, the transport critical current measurement of the barrel samples is carried out in a solenoidal magnet with applied magnetic fields of 7, 8, 9, 10, 11, and 12 T, which is parallel to the axis of the VAMAS barrel; the directions of the applied magnetic field and transport current are shown in Fig. 1(a), and the operating temperature is 4.2 K.

For the magnetization measurement, a VSM is used [12]. After heat treatment, the minicoil sample section with a length of about 8 mm is mounted on an end of a rod holder made from PEEK material and covered with a Teflon tape for fixation, as shown in Fig. 1(b). The magnetic moment of the sample is

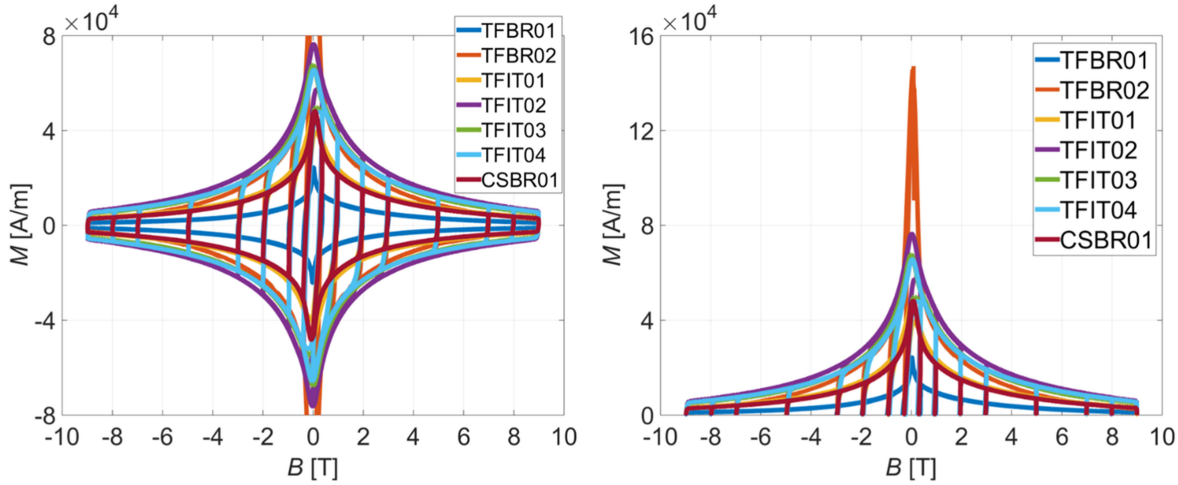

Fig. 2. Magnetization of the seven minicoil-type samples for different magnetic field amplitudes (left) and with emphasis on the upper branch of the loops (right).

measured in VSM by detecting the induced voltage of the two oppositely connected detection coils [13]. The uniform magnetic field applied is parallel to the axis of the minicoil, as seen in Fig. 1(b), and continuously swept between a minimum and maximum magnitude B_m, i.e., between $-B_m$ and $+B_m$, and with a constant change rate (ramp rate r). The employed sequence of the maximum fields B_m is: 0.2, 0.3, 0.4, 0.5, 0.7, 1.0, 2.0, 3.0, 5.0, 7.0, 8.0, and 9.0 T. The ramp rate is $r = 0.07$ T/min for the sweeping field with a maximum magnitude less than or equal to 2.0 T, and $r = 0.5$ T/min for the higher field magnitudes. The testing temperature is also 4.2 K [11]. The magnetization of the strand is derived from the magnetic moment measured and the volume of the sample.

Besides the magnetic field and temperature, the critical current density of the Nb_3Sn superconductor is strongly dependent on the strain applied to the material [14], [15]. The Nb_3Sn composite wire will contract under axial strain after cooling down to 4.2 K and typically contract more in comparison to a Ti6Al4V ITER barrel; it means that the wire will be slightly stretched during cool down on an ITER barrel [16], [17]. Furthermore, the strain stays within a narrow ranging window, and the average values of BR and IT strands are -0.19 and -0.13%, respectively [18]. However, in order to scale the eventual fit parameters to more realistic values, a generic compressive strain state -0.15% is assumed for both the wires in the critical current measurements throughout the analysis in this article. For the minicoils in the magnetization measurements, the thermal expansion coefficient of the PEEK material is higher than the Nb_3Sn [19], [20]; the assembly of the minicoils is slightly loose after the cool down and needs to be fixed with Teflon tape. Thus, the strain in the minicoil is attributed to the precompression exerted by the bronze matrix on the Nb_3Sn filaments and a order of -0.20% is adopted. Both the critical current and magnetization measurements are then corrected with the correct strains.

Considering the demagnetization effect of the VSM, a calibration is performed by using a standard reference sample for comparison [12]. A minicoil is prepared from nickel wire, having a high and well-known saturation moment of 641 mT at 4.2 K [21], [22].

III. Experimental Results

A. Hysteresis Loss

The magnetic moments of the minicoil Nb_3Sn strand samples, as well the nickel minicoil for calibration, are measured for sweeping magnetic field cycles up to 9.0 T. The magnetization is defined as the magnetic moment per unit volume. The magnetization of the seven strand samples versus the applied magnetic field B with different field amplitudes is shown in Fig. 2. The results show that the two TF BR strands exhibit quite distinctive behavior, especially the TFBR02 strand reveals a very high magnetization at low field magnitude range. While, for the four IT processed TF strands, the magnetization behaviors are quite similar.

The area enclosed by the magnetization loop represents the hysteresis loss, as expressed in (1). If the width between the upper and lower branches of the magnetization loop is denoted as $\Delta M(B) = M^+(B) - M^-(B)$, the $\Delta M(B)$ dependence on the magnetic field can be derived from the magnetization loops. The $\Delta M(B)$ plots for two typical strands, TFBR02 and TFIT01, are shown in Fig. 3. The sharp peak of TFBR02 indicates that a very high magnetization is induced at the low field range. Besides, flux jumps occur at the peak, as seen in the inserted zoom in the left plot of Fig. 3. The TFIT01 sample is typical for the other samples; a smoother change of the magnetization is observed passing zero field. Based on the calculation of ΔM, the hysteresis loss of the strand with respect to the magnetic field maximum amplitude B_m is calculated by (2). The hysteresis losses of all the seven samples are shown in Fig. 4, showing that the data of all the strands satisfy the ITER Nb_3Sn maximum criterion for hysteresis loss at B_m of ± 3 T field cycle [6]–[8], as listed in Table I.

$$Q_{\text{hyst}} = \oint M dB \ \left[\text{J/m}^3 \cdot \text{cycle}\right] \tag{1}$$

$$Q_{\text{hyst}}\ (B_m) = 2\int_0^{B_m} \Delta M\,(B)\ dB\ \left[\text{J/m}^3 \cdot \text{cycle}\right] \tag{2}$$

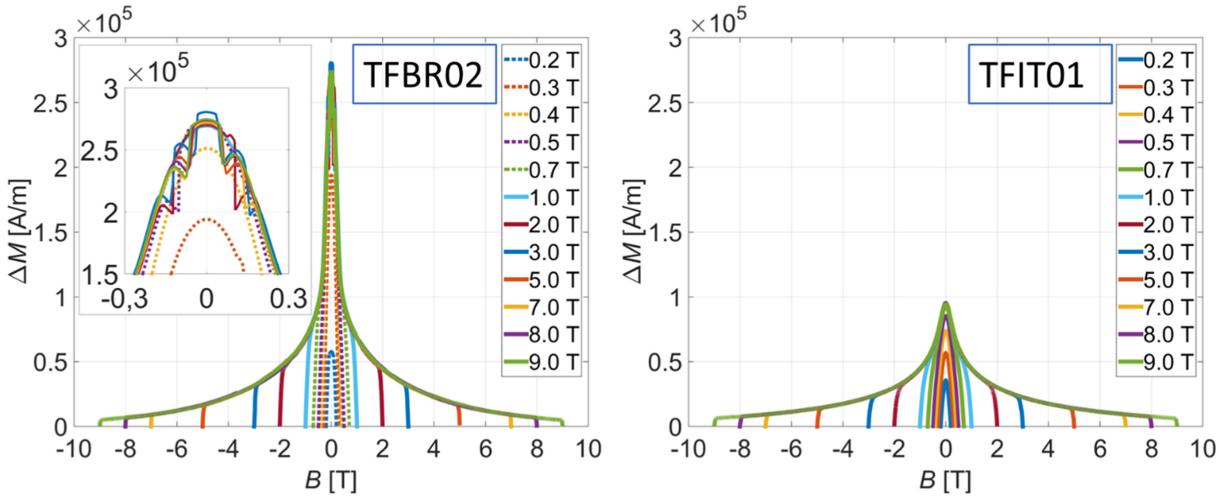

Fig. 3. Delta magnetization ΔM of two typical strand samples, TFBR02 and TFIT01, versus the sweeping magnetic field amplitude. Flux jumps are observed in sample TFBR02, as shown in the inserted zoom of the left plot.

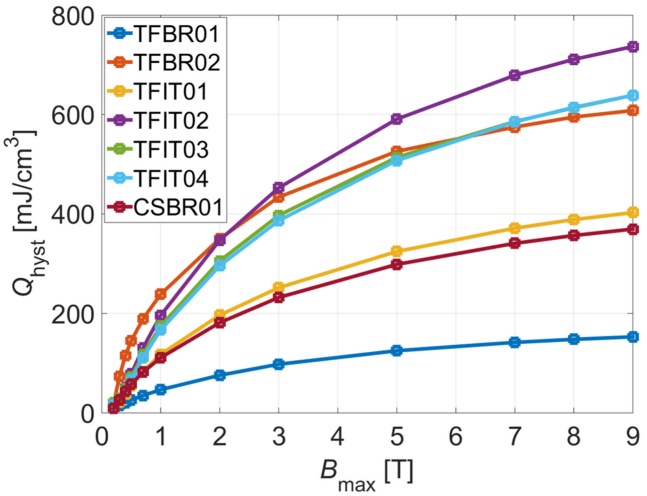

Fig. 4. Hysteresis losses of the seven strand samples versus the applied magnetic field magnitude.

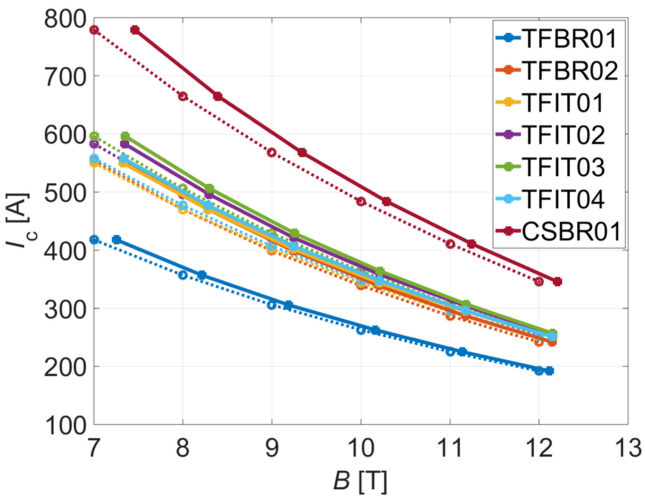

Fig. 5. Self-field correction (solid line) for the critical currents versus field of seven Nb_3Sn strands measured on the standard ITER barrel in comparison with the data without correction (dashed line).

B. Transport Current Measurement and Parameterization

Compared to the magnetization measurements, which describe the strand behavior at $B \leq 9$ T, the transport current measurements are performed at the range $7 \leq B \leq 12$ T. The critical current of the seven ITER samples is measured at 4.2 K, with an electrical field criterion of 10 μV/m in the field range from 7 to 12 T with steps of 1 T. For the ITER barrel-type sample, the self-field generated by the wire cannot be ignored [16] and corrected with (3) [23]

$$B_{\text{corr}} = B_{\text{ext}} + \left(\frac{2}{R} - 0.90\right) I_c \times 10^{-4} \tag{3}$$

with R (in mm) as the radius of the Nb_3Sn filamentary area inside the strand and I_c in A.

The corrected field dependence of the critical current of the seven samples in comparison with original measured data is shown in Fig. 5.

The engineering critical current density is then obtained, $J_{ce} = I_c/S_{\text{total}}$, where S_{total} is the area of the strand cross section. For a cylindrical superconducting strand getting fully penetrated in a perpendicular field, such as the measured ITER multifilamentary superconducting wires, the relation between the magnetization and critical current density can be described by (4) [5], [24], [25].

$$J_{ce} = \frac{3\pi}{4d_{\text{eff}}} \Delta M \tag{4}$$

where d_{eff} is the effective filament size of the strand, regarded as a geometrical proportionality constant between ΔM and J_c. Since both the magnetization and critical current measurements are performed at common magnetic fields of 7, 8, and 9 T, the d_{eff} for the three magnetic fields, as well as the average value, are calculated and shown in Table III. The results show that the impact of the magnetic field and current density on the effective filament diameter is not significant. The average

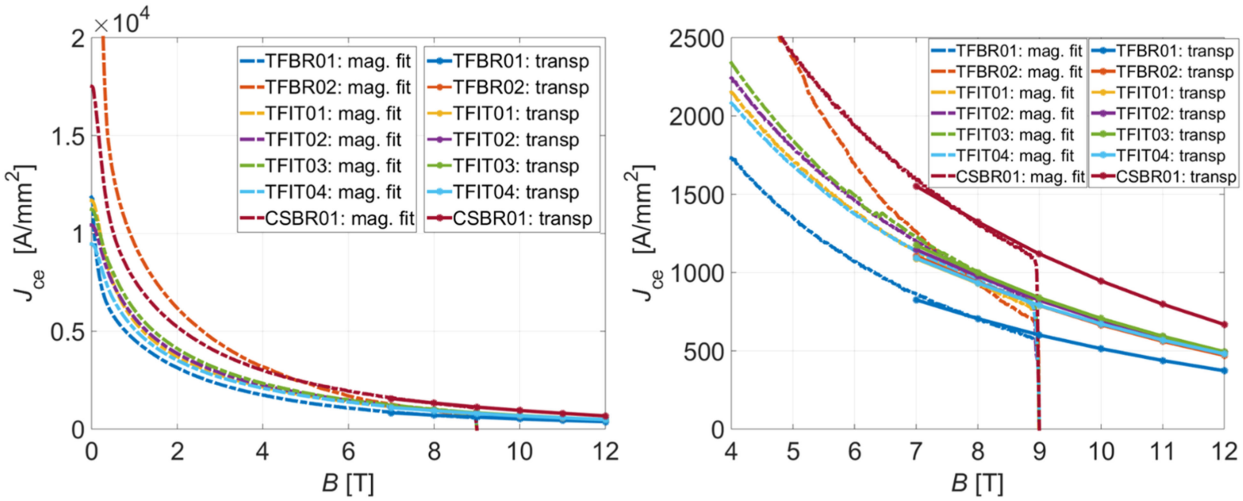

Fig. 6. Evolution of the extended J_{ce} curves at the full field range for the seven samples derived from both the magnetization and transport critical current measurements (left) and coherence of J_{ce} determined by the two types of data sources at the overlapped field region (right).

TABLE III
EFFECTIVE DIAMETER OF THE SEVEN SAMPLES DERIVED FROM THE MAGNETIZATION AND CRITICAL CURRENT MEASUREMENTS AT THE OVERLAPPING MAGNETIC FIELD RANGE

	d_{eff} [μm]			
	B=7.0 T	B=8.0 T	B=9.0 T	Average
TFBR01	9.4	9.1	8.6	9.0 ± 0.4
TFBR02	19.5	16.8	14.8	17.0 ± 2.4
TFIT01	20.1	19.3	18.3	19.2 ± 0.9
TFIT02	36.1	34.9	32.3	34.4 ± 1.9
TFIT03	29.7	28.6	26.7	28.4 ± 1.5
TFIT04	34.1	33.1	30.4	32.5 ± 1.9
CSBR01	13.0	12.6	12.2	12.6 ± 0.4

filament diameter is taken as a constant strand characteristic and used for the extension of $J_c(B)$ at the full magnetic field range. For the magnetization ΔM measured at the field range from 0.2 to 9 T, the corresponding engineering critical current density is derived by means of (4). Together with the values directly derived from the critical current measurements performed at the field range from 7 to 12 T, a normalized J_{ce} relation at the full field range from 0.2 to 12 T is obtained and shown in Fig. 6. In the left plot, the J_{ce} of the TFBR02 sample is increasing further and approaching nearly 4×10^4 A/mm^2 at the lowest field. The right plot emphasizes the coherence of the two types of data sources at the overlapped field region. In general, a fair correlation of the J_{ce} derived from the different sources is observed, which indicates good extension of the $J_c(B)$ at the full magnetic field range. Some deviation observed at the overlapping region is mainly caused by the applied d_{eff}, which is an average value and closer to the value calculated at 8 T, and usually slightly lower than the value at 7 T. However, a relatively poor correlation is observed for the TFBR02 strand, which is most likely due to the impact of the niobium diffusion barrier on the magnetization ΔM.

C. Scaling Law Parameterization

Some empirical relations among the critical current, magnetic field, temperature, and strain of the Nb_3Sn wires are derived based on the descriptions of microscopic mechanisms; however, some of them are relatively complex and use a significant number of parameters to describe the material involved [26], [27]. For the magnetic field dependence of the critical current density in Nb_3Sn wires, it is determined by the depinning of the flux-line lattice and, thus, by the magnetic field dependence of the bulk pinning force $F_p = J_c \times B$. In consideration of a balance between the microscopic interpretation and the practical applicability, the critical current density scaling law is normally obtained by interpolating and extrapolating the measured critical current data. A general description for $F_p(B)$ is like

$$F_p \propto \frac{B_{c2}^{\nu}}{\kappa_1^{\gamma}} f(b) \tag{5}$$

in which b is the reduced magnetic field B/B_{c2}, κ_1 is related to the thermodynamic critical field, both powers ν and γ are regarded as free parameters to allow for errors in the temperature dependences, usually $\nu \approx 2$ and $\gamma \approx 1$ [26], [28].

Based on the magnetization measurements with the VSM and the fact that ΔM is proportional to the critical current density J_c, as also seen in (4), therefore, $F_p = J_c \times B \propto \Delta M \times B$, a fitting function is introduced to analytically describe the $\Delta M(B)$ dependence [5]

$$\Delta M(B) \times B = C\left(\frac{B}{B_{c2}}\right)^{p}\left(1-\frac{B}{B_{c2}}\right)^{q} \tag{6}$$

in which p and q are $f(b)$ related parameters; however, it is divergent at $B = 0$, and thus conflict with the calculation of hysteresis loss, as shown in (1). This problem is solved by introducing a field component B_{int}, which is contributed by the superconducting current circulating inside the sample, and

regarded as a smooth and exponentially decaying function of B

$$B_{\text{int}} = 0.5B_{p0}\exp\left(-\frac{B}{aB_{p0}}\right) \tag{7}$$

Then, an effective magnetic field $B_{\text{eff}} = B + B_{\text{int}}$ is adopted to describe the general scaling relation

$$\Delta M\ (B) = \frac{C}{B+B_{\text{int}}}\left(\frac{B+B_{\text{int}}}{B_{c2}}\right)^{p}\left(1-\frac{B+B_{\text{int}}}{B_{c2}}\right)^{q} \tag{8}$$

Considering the potential effect of the "internal field" B_{int}, the fitting procedure is first applied at relatively high magnetic field region to determine the parameters p, q, and B_{c2}, and then determine the internal field relevant parameters a and B_{p0} by applying magnetic field covers B_{int}. Specifically, three main steps are involved to derive the fitting parameters.

In the first step, as the applied filed is sufficiently higher than the position of the pinning force maximum [27], such as $B > 6$ T, the pinning force F_p is equivalent to the product $\Delta M \times B$, and the effect of B_{int} is ignored, $B_{\text{int}} = 0$. In this region, the shearing of the flux-line lattice is the primary depinning mechanism, and the parameters $p = 0.5$ and $q = 2$ are chosen due to the normally good magnetic field dependence on the entire temperature and strain regime [26], [29], only the parameters C and B_{c2} are left free. In the second step, the $\Delta M \times B$ data at applied fields higher than 1.5 T were considered and fitted; the parameter B_{c2} ought to be fixed to the value determined in the first step; however, considering the effect of the strain and temperature, the B_{c2} is corrected at zero strain and temperature [15], [30], [31] by using the model, $B_{c2}\ (\in) = B_{c2}\ (00)S(\in)(1-t^{1.52})$, in which $S(\in)$ is strain dependence [4], [26], $t = T/T_c(\in)$, and $T_c\ (00) = 16.7$ K [16]. The remaining parameters C, p, and q are left free. While in the third step, the magnetization data ΔM are considered in the full range of the applied field after taking into account the effect of B_{int}. In the fitting procedure of (8), the parameter B_{c2} is still fixed to the corrected value determined previously, and the parameter p mainly defines the shape of the pinning force in the low field region [15] and q affects the maximum pinning force and its position [26]; they are set to the values determined in the second step; thus, only C, B_{p0}, and a are free parameters. By now, all six fitting parameters are obtained.

Except for the TFBR02 strand sample, other six samples are subjected to the three-step fitting procedure as described above. While for the TFBR02 strand, a distinct high magnetization at the low field range is observed, as shown in Figs. 2 and 3. The large difference is related to the diffusion barrier materials, niobium for the TFBR02 strand and tantalum for the other six strands. The diffusion barrier is used to isolate the Cu stabilizer from regions in the conductor, where Sn diffuses to Nb during the reaction heat treatment [32]. Wires with a niobium diffusion barrier usually generate higher hysteresis loss than the ones with a tantalum barrier [33]. Since the B_{c2} of pure niobium at 4.2 K is about 0.3–0.4 T [34], the superconductivity of the niobium diffusion barrier affects the magnetization behavior below B_{c2}. By contrast, the effect of a tantalum barrier works only below 0.1 T [35]. Thus, the impact of the superconducting niobium barrier should be considered during the scaling law fitting of the TFBR02 strand. A threshold value B_{th}, close to B_{c2}, is set to determine the effective contribution of the superconducting niobium barrier. The contribution is considered to be negligible if the magnetic field exceeds B_{th}; otherwise, the total magnetization is contributed by the Nb_3Sn and Nb components simultaneously. The contribution of Nb_3Sn at the low field region $B_{\min} < B < B_{\text{th}}$ is derived by an extrapolation of the $\Delta M(B)$ curve from the field regime $B_{\text{th}} < B < B_{\max}$, then the corresponding contribution of the Nb is defined as $\Delta M_{\text{Nb}}(B) = \Delta M_{\text{total}}(B) - \Delta M_{\text{Nb3Sn}}(B)$. In practice, the extrapolation line is tangential to the ΔM curve at the field B_{th}; thus, it is sensitive to the curvature and evolution of the curve. An engineering B_{th} value of 0.55 T, which is slightly higher than B_{c2}, is determined from a smooth and optimal extrapolation. The contribution of the Nb_3Sn and Nb components on the magnetization ΔM is shown in Fig. 7 in which the green point corresponds to the threshold field B_{th}.

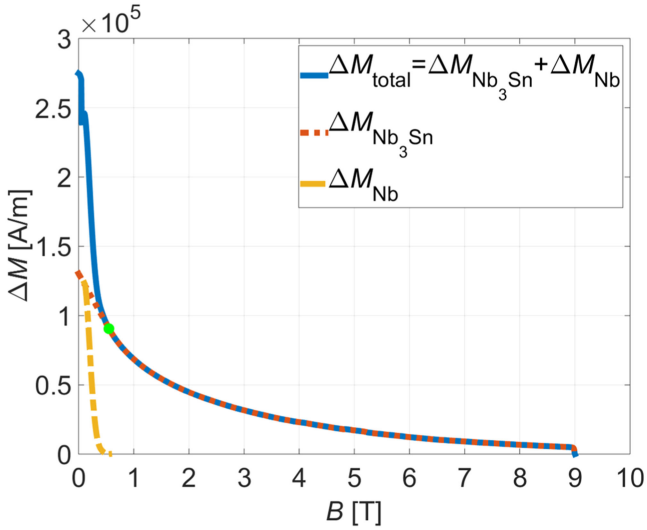

Fig. 7. Contribution of the Nb_3Sn and Nb on the magnetization of the TFBR02 strand with Nb diffusion barrier; the green point represents B_{th}, which indicates the beginning of the extrapolation line.

For the TFBR02 strand, the ΔM fitting of the Nb_3Sn and Nb components are executed in the field range of $0.55 \le B \le 9$ T and $0 \le B < 0.55$ T, respectively. The fitting process of the Nb_3Sn contribution follows the three-step method as described above, while the fitting of the Nb contribution considers only the last step, except the parameter q, which is fixed to 2, and all the other parameters are left free.

For the VSM magnetization measurement, a set of ΔM data is derived directly with magnetic field up to 9 T. Furthermore, according to (4), the $J_{ce}(B)$ relation is extended at the full magnetic field range from 0 to 12 T; a set of extended $\Delta M(B)$ data is then obtained correspondingly. However, the transport current measurements are only performed at six magnetic fields, far less than the thousands of sampled data derived from the magnetization measurements. Therefore, an interpolation is applied to the six ΔM data curves from the transport measurements to obtain a similar data density as for the VSM magnetization measurement. This way an appropriate dependency is achieved on the weight of sampling points for the fitting routine. The deviation between the

TABLE IV
SUMMARIZED ZERO-TEMPERATURE UPPER CRITICAL FIELD B_{c2} DERIVED FROM THE FIRST FITTING STEP WITH DIFFERENT EXPERIMENTAL DATA SOURCES

	TFBR01	TFBR02	TFIT01	TFIT02	TFIT03	TFIT04	CSBR01
ΔM data fit	24.80	18.31	25.83	26.21	25.58	28.23	26.55
$\Delta M + I_c$ data fit	30.27	25.09	29.74	28.63	28.87	29.68	29.75
I_c data fit	32.53	30.32	31.96	30.44	29.92	31.38	30.65

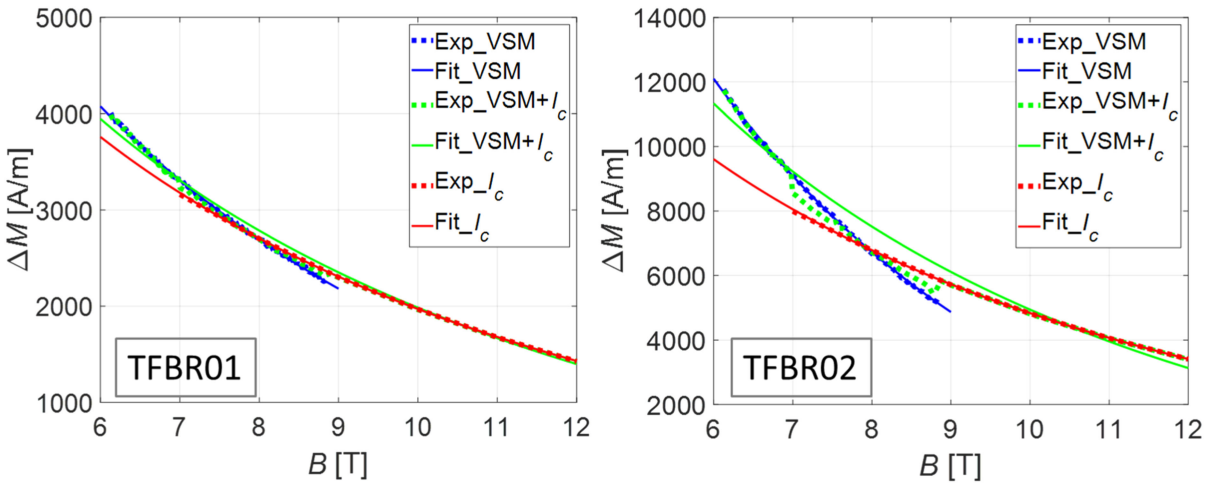

Fig. 8. Fitting the experimental ΔM data from different measurements in the first step to obtain the B_{c2} parameter for TFBR01 and TFBR02 strand samples, respectively.

two datasets at the overlapped magnetic field region, as observed in the right plot of Fig. 6, is treated with a smoothing and sparse processing method.

After the necessary data preprocessing, these two ΔM datasets are optimized, with a maximum magnetic field up to 9 T and 12 T, respectively. The three-step fitting process are performed on the ΔM datasets individually to obtain the scaling parameters. The zero-temperature upper critical field B_{c2} derived from the first fitting step is summarized in Table IV. In contrast to the relatively large range of difference in critical current density, the upper critical field B_{c2} of the ternary Nb_3Sn strands is strikingly similar, reaching to 30 T or slightly higher [30], [36], [37]. However, as seen in Table IV, for all samples, the B_{c2} derived from fitting the VSM experimental data is lower than the empirical value, while the ones derived from fitting the combined VSM and I_c experiments are reasonable, except the TFBR02 sample, of which B_{c2} is 18.31 T and 25.09 T, respectively; both are lower than the empirical value and not comparable to the other samples. The first step fitting curves with respect to different experimental ΔM data sources are shown in Fig. 8 for TFBR01 and TFBR02 strand samples, respectively. In addition, the fitting curve of the ΔM data derived from I_c measurement alone is also included.

Similar to the coherence deviation at the overlapping region between VSM and I_c datasets, as shown in Fig. 6, deviation between the three fitting curves is also observed, especially for the TFBR02 strand sample. The fitting curve behaviors of the other six strands are quite similar and the TFBR01 sample is selected as a representative. The B_{c2} values derived from two fitting curves, which correspond to the combined data of VSM and I_c measurements or the I_c data alone, respectively, are in the range of the empirical values [30], [38], while, for the TFBR02, only the value derived from the I_c measurement is reasonable. The evaluation of the B_{c2} also implies that the deviation between the VSM and I_c data is most probably attributed to the VSM data, such as the inaccuracy related to the measurement or data process, or the impact of the niobium diffusion barrier for the TFBR02 sample. In consideration of the underestimation of the B_{c2}, it is not suitable to use the measured VSM data alone for parameterization in the first step fitting. Considering the empirical B_{c2} values and the experimental data coherence, the ΔM data derived from the I_c measurement for TFBR02 and the data derived from both the VSM and I_c measurements for the other six samples are chosen for the first step fitting procedure to obtain the B_{c2} parameters.

Regarding the TFBR02 sample with the niobium diffusion barrier, the fitting is processed separately for the very low field region. For the Nb_3Sn component of the TFBR02 strand as well as for the other six strands, the final fitting curves (third step) in comparison with the extended experimental magnetization curves are shown in Fig. 9; the good fits are observed for all samples. The fitting result of the niobium diffusion barrier of the TFBR02 strand is shown in Fig. 10. The scaling law fitting parameters for both Nb_3Sn and Nb contributions are summarized in Table V in which the parameter p mainly defines the shape of the pinning force in the low field region and q is the higher field shaper parameter and affects the maximum pinning force and its position.

TABLE V
ΔM FITTING PARAMETERS FOR MAGNETIZATION DATA AT FIELD RANGE FROM 0 TO 12 T

Parameter		$C/10^5$ [T·A/m]	B_{c2} [T]	p [-]	q [-]	B_{p0} [T]	a [-]
TFBR01	Nb_3Sn	0.880	30.27	0.409	2.628	0.701	2.7471
TFBR02	Nb_3Sn	5.591	30.32	0.551	4.867	0.597	1.473
	Nb	0.740	0.467	0.100	2.000	0.451	0.230
TFIT01	Nb_3Sn	2.815	29.74	0.498	2.682	0.444	2.701
TFIT02	Nb_3Sn	5.179	28.63	0.500	2.569	0.701	1.251
TFIT03	Nb_3Sn	4.056	28.87	0.457	2.529	0.701	1.711
TFIT04	Nb_3Sn	4.850	29.68	0.526	2.636	0.624	1.429
CSBR01	Nb_3Sn	2.319	29.75	0.460	2.481	0.663	1.921

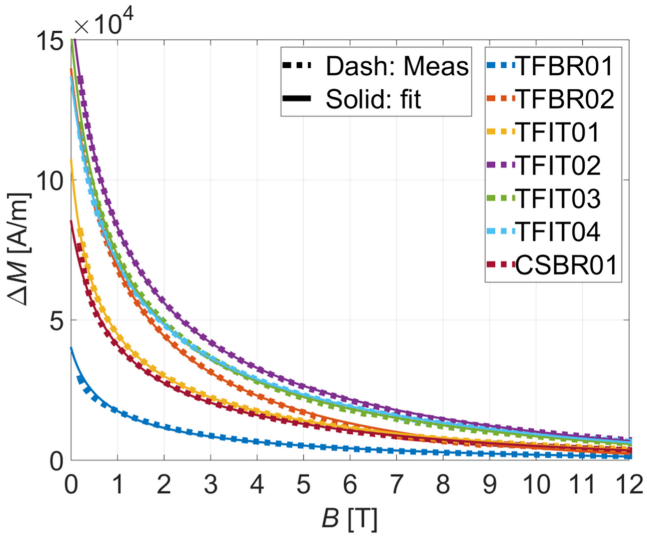

Fig. 9. Scaling law function fitting with the extended experimental magnetization ΔM at the full field range from 0 to 12 T.

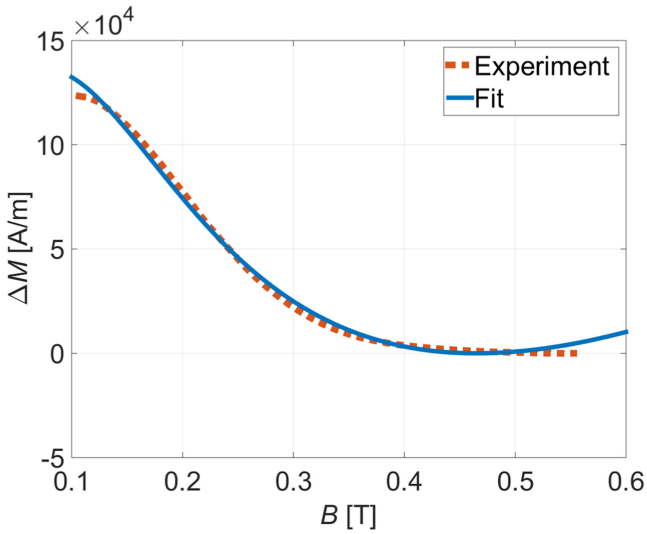

Fig. 10. Scaling law fitting of the magnetization component contributed by the niobium diffusion barrier of the TFBR02 strand.

IV. DISCUSSION

As observed in Table V, except the TFBR02 sample, the values of $p \approx 0.5$ and $q \approx 2.5$ are derived for all the other samples, which are close to the empirical values of 0.5 and 2.0, respectively. The $\pm 25\%$ variation of q mainly changes the maximum pinning force and its position, and a larger q implies a reduced maximum pinning force with a shift of its position toward the lower magnetic field [26]. Since the different values of p and q implicate a different pinning behavior, and most probably originate from inhomogeneity averaging, therefore, the particularly high value of $q \approx 4.9$ of the TFBR02 sample seems to imply a severe inhomogeneity. However, this fitted high value is determined by compounded factors, especially the measured high magnetization, and the discrepancy between the normalized magnetization and transport current data.

For each tested strand, besides the minicoil and VAMAS samples, a straight sample is prepared as well and heat treated at the same time. In terms of the magnetization measurements, two types of samples in minicoil and short–straight shapes are tested for mutual validation. A good coherence is observed between the measured magnetizations, including the TFBR02 strand, which, therefore, excludes the possibility of inappropriate sample preparation and testing mistakes.

TABLE VI
CHARACTERISTICS OF THREE BR PROCESSED Nb_3Sn STRANDS, $*$ - DATA DERIVED FROM MICROSCOPE IMAGE AT UNIVERSITY OF TWENTE (UT); $**$ - DATA PROVIDED BY ITER INTERNATIONAL ORGANIZATION.

Sample	N_{fil}	d_{fil} [μm]	Barrier	Barrier thickness [μm]	
				UT *	ITER **
TFBR01	8305	4.7 *	Ta	~14.1 *	~
TFBR02	12787	2.8 **	Nb	~10.2 *	7.0 **
CSBR01	17347	3.0 *	Ta	~10.3 *	~

N_{fil} is the number of filaments.

Furthermore, considering the probable influence of the heat treatment, a microscope examination is performed on the strands, and the cross sections of the three bronze processed strands (TFBR01, TFBR02, and CSBR01) are shown in Fig. 11. Due to the limitation of the microscope resolution, the grain morphology of the Nb_3Sn strands after heat treatment cannot be distinguished. However, no unusual behaviors are observed based on the filament level images after zooming.

There are many factors affecting the strand behaviors, such as the content and gradient of Nb and Sn [39], heat treatment [40], filament diameter, filament spacing, and diffusion barrier material. The specifications of these three strands are listed in Table VI in which the TFBR02 and CSBR01 strands have a

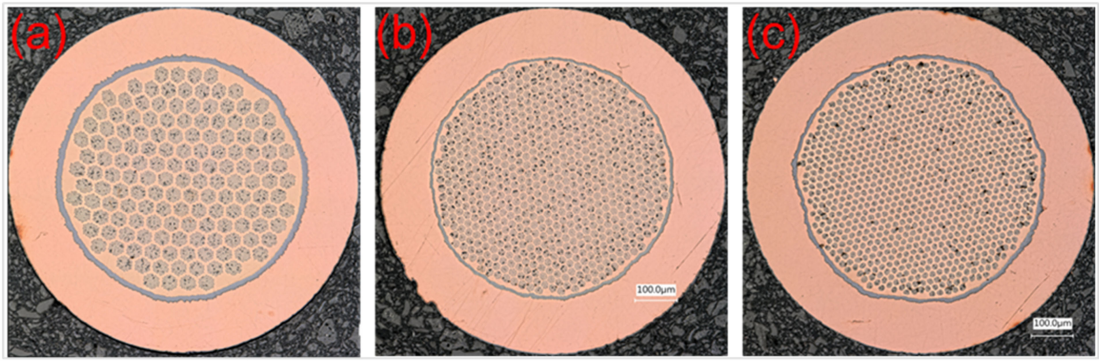

Fig. 11. Microscope images of the cross sections of three bronze routed Nb_3Sn strands. (a) TFBR01. (b) TFBR02. (c) CSBR01 strand samples.

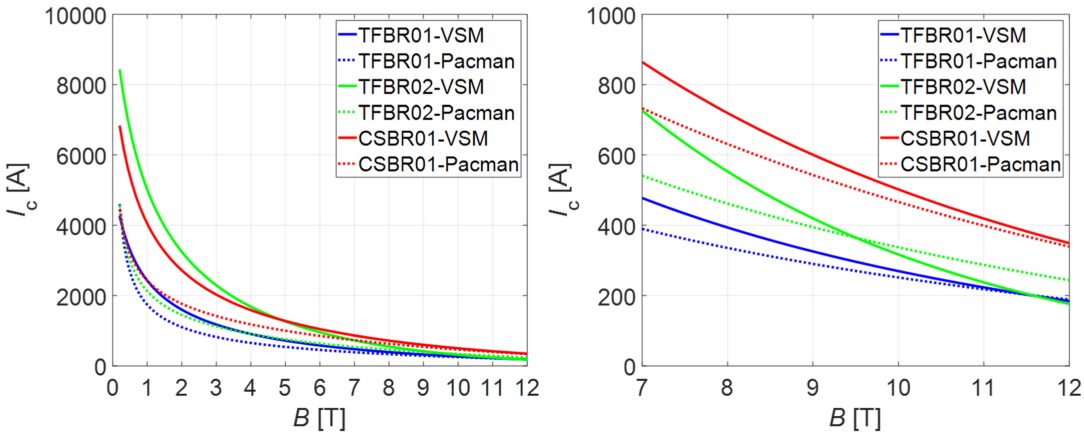

Fig. 12. (left) Comparison between the critical currents derived from the VSM and Pacman measurements; the strands are provided by the same suppliers but from different batches. (right) Zoom-in plot at the main field range of Pacman I_c measurement.

similar filament diameter (d_{fil}) and diffusion barrier thickness, and both were subjected to the same heat treatment. The larger amount of filaments (N_{fil}) of the CSBR01 strand implies a smaller filament spacing and, thus, could be more sensitive to the proximity effect [41]; nevertheless, CSBR01 still shows a "better" scaling law fitting. A plausible explanation for this particular characteristic of the TFBR02 strand is the presence of the niobium diffusion barrier. It is possible that an Nb_3Sn layer is formed on the internal surface of the barrier. This way the barrier itself becomes an active path for the screening currents and increases the losses significantly, even in the case in which the applied field exceeds the penetration field [42], [43]. In that case, the hysteresis losses are dependent on the thickness of the Nb component layers [41].

Another possiblity for the extraordinary behavior of the TFBR02 strand is the sample itself, which might be defective and, thus, not representative. In the case of lacking of investigation on the Nb_3Sn grain morphology, a simple verification is performed by comparing the historical database, such as the TARSIS and Pacman $I_c(\epsilon)$ tests [18], [44], [45]. After normalized to the I_c data, a comparison between the results derived from the VSM and Pacman measurements is shown in Fig. 12, corresponding to the three bronze routed strands too. A largest discrepancy is observed at the low field region for the TFBR02 sample; it seems the present strand used for the VSM measurement is not representative. However, it should be mentioned here that the Pacman measurements were performed in the magnetic field range of 6 to 14 T; the Pacman curves at the field below 6 T are extrapolated according to the scaling law [18], and it is not accurate enough and might be underestimated; thus, the discrepancy between VSM and Pacman data sources should be narrowed; actually, this is one of the main targets of the work described in this article.

With respect to the different performance of the experiments and scaling law parameterization of TFBR02 sample, there are two probable reasons but not definitely confirmed, leading to still ongoing research and discussion.

V. Conclusion

In order to obtain a practical scaling law of the ITER Nb_3Sn strands, in the normally operating field region lower than 4 T, a series of magnetization and transport current measurements of seven ITER Nb_3Sn strands are performed in which the magnetizations are measured in field region up to 9 T, while the transport current of the samples is measured at field from 7 to 12 T; since the transport current density is proportional to the magnetization, it is able to combine these two series of tests through the common field region from 7 to 9 T, and the scaling law is derived by fitting the $\Delta M(B)$ at the full field region up to 12 T. Four IT processed samples and two bronze routed samples with tantalum diffusion barriers exhibit good fitting behaviors,

but for the bronze routed sample with niobium diffusion barrier, an extremely high ΔM at low field region is observed, leading to a large deviation of the fitting curve. The fitting procedure is improved by separating the Nb and Nb_3Sn components at the low field region.

V. Disclaimer

The views and opinions expressed herein do not necessarily reflect those of the ITER Organization.

References

[1] N. Mitchell et al., "The ITER magnet system," *IEEE Trans. Appl. Supercond.*, vol. 18, no. 2, pp. 435–440, Jun. 2008.

[2] N. Mitchell, A. Devred, P. Libeyre, B. Lim, and F. Savary, "The ITER magnets: Design and construction status," *IEEE Trans. Appl. Supercond.*, vol. 22, no. 3, Jun. 2012, Art. no. 4200809.

[3] A. Devred et al., "Challenges and status of ITER conductor production," *Supercond. Sci. Technol.*, vol. 27, 2014, Art. no. 044001.

[4] L. Bottura and B. Bordini, "$J_c(B,T,strain)$ parameterization for the ITER Nb_3Sn production," *IEEE Trans. Appl. Supercond.*, vol. 19, no. 3, pp. 1521–1524, Jun. 2009.

[5] E. Seiler et al., "Hysteresis losses and effective $J_c(B)$ scaling law for ITER Nb_3Sn strands," *IEEE Trans. Appl. Supercond.*, vol. 26, no. 2, Mar. 2016, Art. no. 8200307.

[6] A. Devred et al., "Status of ITER conductor development and production," *IEEE Trans. Appl. Supercond.*, vol. 22, no. 3, Jun. 2012, Art. no. 4804909.

[7] A. Vostner et al., "Statistical analysis of the Nb_3Sn strand production for the ITER toroidal field coils," *Supercond. Sci. Technol.*, vol. 30, 2017, Art. no. 045004.

[8] T. Boutboul et al., "European Nb_3Sn superconducting strand production and characterization for ITER TF coil conductor," *IEEE Trans. Appl. Supercond.*, vol. 26, no. 4, Jun. 2016, Art. no. 6000604.

[9] K. Tachikawa and P. J. Lee, "History of Nb_3Sn and related A15 wires," in *100 Years of Superconductivity*. Boca Raton, FL, USA: CRC Press, 2011, pp. 661–671.

[10] P. Bruzzone, H. H. J. ten Kate, M. Nishi, A. Shikov, J. Minervini, and M. Takayasu, "Bench mark testing of Nb_3Sn strands for the ITER model coil," in *Advances in Cryogenic Engineering Materials*, vol. 42. New York, NY, USA: Springer, 1995, pp. 1351–1358.

[11] A. Nijhuis, W. A. J. Wessel, Y. Ilyin, A. den Ouden, and H. H. J. ten Kate, "Critical current measurement with spatial periodic bending imposed by electromagnetic force on a standard test barrel with slots," *Rev. Sci. Instrum.*, vol. 77, 2006, Art. no. 054701.

[12] S. Foner, "The vibrating sample magnetometer: Experiences of a volunteer (invited)," *J. Appl. Phys.*, vol. 79, pp. 4740–4745, 1996.

[13] S. Foner, "Versatile and sensitive vibrating-sample magnetometer," *Rev. Sci. Instrum.*, vol. 30, pp. 548–557, 1959.

[14] A. Godeke, F. Hellman, H. H. J. ten Kate, and M. G. T. Mentink, "Fundamental origin of the large impact of strain on superconducting Nb_3Sn," *Supercond. Sci. Technol.*, vol. 31, 2018, Art. no. 105011.

[15] B. Bordini, P. Alknes, L. Bottura, L. Rossi, and D. Valentinis, "An exponential scaling law for the strain dependence of the Nb_3Sn critical current density," *Supercond. Sci. Technol.*, vol. 26, 2013, Art. no. 075014.

[16] A. Godeke et al., "A review of conductor performance for the LARP high-gradient quadrupole magnets," *Supercond. Sci. Technol.*, vol. 26, 2013, Art. no. 095015.

[17] A. K. Ghosh, "Effect of barrel material on critical current measurements of High-J_c RRR Nb_3Sn wires," *IEEE Trans. Appl. Supercond.*, vol. 21, no. 3, pp. 2327–2330, Jun. 2011.

[18] A. Nijhuis et al., "The effect of axial and transverse loading on the transport properties of ITER Nb_3Sn strands," *Supercond. Sci. Technol.*, vol. 26, 2013, Art. no. 084004.

[19] D. P. Boso and M. Lefik, "A thermo-mechanical model for Nb_3Sn filaments and wires: Strain field for different strand layouts," *Supercond. Sci. Technol.*, vol. 22, 2009, Art. no. 125012.

[20] 2019. [Online]. Available: https://dielectricmfg.com/knowledge-base/peek/

[21] D. R. Lide, *CRC Handbook of Chemistry and Physics*. New York, NY, USA: Taylor & Francis, 2004.

[22] R. M. Bozorth, *Ferromagnetism*. Piscataway, NJ, USA: IEEE Press, 1978.

[23] B. Bordini, "Self-field correction in critical current measurements of superconducting wires tested on ITER VAMAS barrels," EDMS, Lestrem, France, Tech. Rep. 1105765, Nov. 2010.

[24] M. D. Sumption, X. Peng, E. Lee, X. Wu, and E. W. Collings, "Analysis of magnetization, ac loss, and d_{eff} for various internal-Sn based Nb_3Sn multifilamentary strands with and without subelement splitting," *Cryogenics*, vol. 44, no. 10, pp. 711–725, 2004.

[25] B. Bordini, D. Richter, P. Alknes, A. Ballarino, L. Bottura, and L. Oberli, "Magnetization measurements of high-J_c Nb_3Sn strands," *IEEE Trans. Appl. Supercond.*, vol. 23, no. 3, Jun. 2013, Art. no. 7100806.

[26] A. Godeke, B. ten Haken, H. H. J. ten Kate, and D. C. Larbalestier, "A general scaling relation for the critical current density in Nb_3Sn," *Supercond. Sci. Technol.*, vol. 19, pp. R100–R116, 2006.

[27] E. J. Kramer, "Scaling laws for flux pinning in hard superconductors," *J. Appl. Phys.*, vol. 44, pp. 1360–1370, 1973.

[28] W. A. Fietz and W. W. Webb, "Hysteresis in superconducting alloys—Temperature and field dependence of dislocation pinning in niobium alloys," *Phys. Rev.*, vol. 178, pp. 657–667, 1969.

[29] L. D. Cooley, P. J. Lee, and D. C. Larbalestier, "Changes in flux pinning curve shape for flux-line separations comparable to grain size in Nb_3Sn wires," *AIP Conf. Proc.*, vol. 614, pp. 925–932, 2002.

[30] A. Godeke, M. C. Jewell, C. M. Fischer, A. A. Squitieri, P. J. Lee, and D. C. Larbalestier, "The upper critical field of filamentary Nb_3Sn conductors," *J. Appl. Phys.*, vol. 97, 2005, Art. no. 093909.

[31] D. M. J. Taylor and D. P. Hampshire, "The scaling law for the strain dependence of the critical current density in Nb_3Sn superconducting wires," *Supercond. Sci. Technol.*, vol. 18, pp. S241–S252, 2005.

[32] K. T. Hartwig, S. Balachandran, R. E. Barber, T. Pyon, and R. B. Griffin, "Design aspects of dual Nb-Ta sheet diffusion barriers for Nb_3Sn conductors," *IEEE Trans. Appl. Supercond.*, vol. 21, no. 3, pp. 2563–2566, Jun. 2011.

[33] J. C. McKinnell, P. M. OLarey, P. D. Jablonski, and M. B. Siddall, "Tantalum-niobium alloy diffusion barriers for superconducting Nb_3Sn wires in fusion applications," in *Advances in Cryogenic Engineering Materials*, vol. 42, L. T. Summers, Ed. Boston, MA, USA: Springer, 1996.

[34] D. K. Finnemore, T. F. Stromberg, and C. A. Swenson, "Superconducting properties of high-purity niobium," *Phys. Rev.,* vol. 149, pp. 231–243, 1966.

[35] R. W. Shaw, D. E. Mapother, and D. C. Hopkins, "Critical fields of superconducting tin, indium, and tantalum," *Phys. Rev.*, vol. 120, pp. 88–91, 1960.

[36] A. Godeke, B. Ten Haken, and H. H. J. ten Kate, "Toward an accurate scaling relation for the critical current in niobium-tin conductors," *IEEE Trans. Appl. Supercond.*, vol. 12, no. 1, pp. 1029–1032, Mar. 2002.

[37] Y. Ilyin, A. Nijhuis, and E. Krooshoop, "Scaling law for the strain dependence of the critical current in an advanced ITER Nb_3Sn strand," *Supercond. Sci. Technol.*, vol. 20, pp. 186–191, 2007.

[38] A. Godeke, M. C. Jewell, A. A. Golubov, B. Ten Haken, and D. C. Larbalestier, "Inconsistencies between extrapolated and actual critical fields in Nb_3Sn wires as demonstrated by direct measurements of H_{c2}, $H*$ and T_c," *Supercond. Sci. Technol.*, vol. 16, pp. 1019–1025, 2003.

[39] L. D. Cooley, C. M. Fischer, P. J. Lee, and D. C. Larbalestier, "Simulations of the effects of tin composition gradients on the superconducting properties of Nb_3Sn conductors," *J. Appl. Phys.*, vol. 96, no. 4, pp. 2122–2130, 2004.

[40] Y. Nabara et al., "Optimization of heat treatment of Japanese Nb_3Sn conductors for toroidal field coils in ITER," *IEEE Trans. Appl. Supercond.,* vol. 24, no. 3, Jun. 2014, Art. no. 6000605.

[41] V. Pantsyrny, A. Shikov, and A. Vorobieva, "Nb_3Sn material development in Russia," *Cryogenics*, vol. 48, pp. 354–370, 2008.

[42] E. N. Popova, I. L. Deryagina, and E. G. Valova-Zaharevskaya, "The Nb_3Sn layers formation at diffusion annealing of Ti-doped multifilamentary Nb/Cu-Sn composites," *Cryogenics*, vol. 63, pp. 63–68, 2014.

[43] A. Nijhuis, H. G. Knoopers, and H. H. J. ten Kate, "The influence of the diffusion barrier on the AC loss of Nb_3Sn superconductors," *Cryogenics*, vol. 34, pp. 547–550, 1994.

[44] K. A. Yagotintsev et al., "Overview of verification tests on ac loss, contact resistance and mechanical properties of ITER conductors with transverse loading up to 30 000 cycles," *Supercond. Sci. Technol.*, vol. 32, 2019, Art. no. 105015.

[45] A. Nijhuis, R. Lubkemann, H. J. G. Krooshoop, and W. A. J. Wessel, "Results of TARSIS and Pacman $I_c(strain)$ testing on Jastec TF Nb_3Sn strand," Univ. Twente, Enschede, The Netherlands, ITER Contract UT-ITER/CT/08/1262, 2011.